11-9-2006

Evidence for Two Kinematically Distinct Broad Emission Line Producing Regions in Active Galactic Nuclei

Stephanie A. Snedden
University of Nebraska-Lincoln, snedden@apo.nmsu.edu

C. Martin Gaskell
University of Nebraska-Lincoln, mgaskell@ucsc.edu

(Submitted to ApJ – comments welcome)

Evidence for Two Kinematically Distinct Broad Emission Line Producing Regions in Active Galactic Nuclei

Stephanie A. Snedden[1]

and

C. Martin Gaskell

Department of Physics and Astronomy, University of Nebraska, Lincoln, NE 68588-0111

snedden@apo.nmsu.edu

mgaskell1@unl.edu

ABSTRACT

We present the results of an analysis of line profiles of high- and low-ionization broad emission lines in 8 AGNs observed by the Hubble Space Telescope. We derive the physical conditions in the gas as a function of velocity. We find no evidence for a separate intermediate line region. For the broad line region as a whole we find a major contradiction between the velocity dependencies of conditions deduced from the major high-ionization lines and those deduced from the hydrogen lines alone if they are assumed to come from the same gas clouds. The hydrogen lines imply that the density decreases with decreasing velocity and the ionizing flux on the gas also decreases with decreasing velocity, while both the density and the ionizing flux deduced from the high-ionization lines are independent of the velocity. We believe that there are two kinematically distinct components of the BLR. The change in ionizing flux implied by the hydrogen lines is consistent with virialization of the motions of the gas producing the low-ionization lines and with the flux falling off as the inverse square of the distance from the central engine. The density of the gas must therefore increase towards the central engine. The velocity-independence of conditions inferred from the high-ionization lines can only be explained if the velocity of the high-ionization gas is independent of distance from the central source. This implies that the motions of this gas cannot be gravity dominated and arise instead in a radiatively-driven outflow.

[1]Current address: Apache Point Observatory, 2001 Apache Point Rd., Sunspot, NM 88349-0059

Subject headings: galaxies: active — quasars: emission lines — line: formation — quasars: general — line: profiles — galaxies: Seyfert

1. Introduction

Early studies and most more recent studies of physical conditions in the broad-line regions (BLRs) of AGNs have been based on integrated fluxes from the major emission lines (e.g., Davidson 1972, 1977; MacAlpine 1974, Baldwin & Netzer, 1978; Kwan & Krolik, 1979; Brotherton et al., 1994). It has been known for some time, however, that the shape of broad emission line profiles varies within the same object, depending on the ionization level of the species producing the line (see references in Snedden & Gaskell 2004; hereinafter "paper 1"). Because of these profiles differences, there *must* be velocity-dependent differences in the physical conditions.

In paper 1 we argued that not only the low-velocity gas, but also the high velocity gas must both be predominantly optically thick (see also Korista & Goad, 2004). In the present paper we look at the conditions in the BLR as a function of projected velocity by modeling line ratios across the emission line profiles. Our aim is to investigate the structure and conditions in the BLR gas that produces the high-ionization lines.

2. Data Analysis

In paper 1 we defined a small sample of AGNs for which Stirpe (1990, 1991) gave high-quality, high-resolution Balmer line profiles and for which comparable quality *Hubble Space Telescope* spectra were available. Stirpe (1990) has given a detailed discussion of the de-blending. Both raw and de-blended, continuum-subtracted Hα and Hβ profiles are given in Stirpe (1990, 1991) along with a detailed discussion of the de-blending.

For the *HST FOS* spectra we fitted and subtracted a power-law continuum. Although the overall continua of AGNs are more complex than this, over the range of 1200 - 2000 Å, which contains the UV emission lines used in our analysis, a single power law is a good fit to the continuum. The best-fit power-law parameters are summarized in Table 1. If the fit is not perfect, this would raise the uncertainty in the calculation of the line ratios, especially in the wings of the lines, where line fluxes are small.

The strongest contaminating feature near Lyα is from N Vλ1240. This feature was fit with a single Gaussian and subtracted from the profile. If a residual signature in the profile after the subtraction was evident, a two-Gaussian fit was made. The feature is quite broad, and it is possible that even with a two-component fit, a very broad component would not be noticed in the residual profile. This could cause a systematic overestimation of the flux of the Lyα red wing at the 20% level. The difficulty in de-blending the red wing of Lyα has been discussed in paper 1.

Intrinsic Lyα absorption features were fit with single Gaussians and removed. The resulting profile was examined for any residual features. A smooth residual across the deblended section was taken as evidence that the Gaussian fit was good. Geocoronal Lyα emission was also fit with a single Gaussian and then subtracted from the profile. When apparent, N V absorption was also removed from Lyα in a similar manner. One of our objects (PG 1351+640) showed very broad N V absorption that was difficult to fit. This could well affect the line ratios on the red side of the emission line peak for that object.

He II λ1640 and O III] λ1663 were deblended and subtracted from C IV. Absorption lines from C IV doublets blueshifted from the emission line peak, were also fit with Gaussians and subtracted. These absorption features arise from within both the AGN and our own galaxy, so multiple features with different redshifts often have to be removed. They are narrow features and errors in the subtraction would only affect a tiny fraction of the emission line profile.

Si III] λ1892 was fit with a single Gaussian and removed from C III].

3. Reddening

The calculation of physical conditions from the fluxes of different emission lines at quite different wavelengths can be significantly affected by reddening. De-reddening AGNs is complicated by variations in the dust properties in AGNs and their host galaxies. These variations result in a variety of reddening curves (see Gaskell et al. 2004). To correct for reddening, estimates of intrinsic plus Galactic reddening were made using measurements of He II λ1640 and λ4684. Of the available diagnostic emission lines, He II was chosen because flux measurements are available from many sources in the literature for the objects in our sample. This allowed us to determine an "average" reddening for each object in the sample, which was necessary, since the optical and UV spectra were obtained at different epochs. The calculation of intrinsic plus Galactic reddening was made using the following relation:

$$E(B-V) = 0.645 \log[7.0 I_{4684}/I_{1640}] \qquad [1]$$

This assumes an intrinsic He II $\lambda1640/\lambda4686$ ratio of ~ 7 (Seaton 1978) and a Galactic reddening curve (e.g., Seaton 1979; Cardelli, Clayton & Mathis, 1989). Table 2 lists a compilation of reddenings derived from the He II lines for our sample. In Table 3 we summarize the minimum, average, and maximum values.

In all but one of these cases from the literature, (the 1984 Ward & Morris measurement for NGC 3783), the optical and UV spectra were obtained at different epochs, and line variability affects the results. Consequently, one can only attempt to get a range of reddening values for each of the objects in our sample.

A direct measurement of reddening was also made from the He II $\lambda1640$ and $\lambda4684$ emission lines in the spectra of NGC 5548. This AGN had undergone extensive monitoring as part of an *International AGN Watch* monitoring campaign, and simultaneous *HST FOS* and optical spectra were obtained over the course of several weeks. A value of $E(B-V) = 0.25$ was calculated for NGC 5548, using Equation 1. Note that this falls between the average and maximum values obtained from the literature and summarized in Table 3.

Although a variety of sources in the literature were used to determine reddening, it is still not possible to be certain that the correct total reddening has been found for each object. This is because the total number of observations per object at different epochs is small. To obtain a better estimate, a much larger number of observations at different epochs is needed, but these are not yet available. Better yet, a series of simultaneous UV and optical observations could ascertain the range of intrinsic reddening, but to date, we only have simultaneous observations in both UV and optical for NGC 3783 and NGC 5548.

It can be seen from Table 2 that in several cases, no evidence of intrinsic reddening was seen based on the He II fluxes found in the literature. This could be real (i.e., there is no intrinsic reddening in the AGN), but it could also be a result of poor He II measurements or the non-simultaneous nature of the measurements of the UV and optical lines. Only one of the objects, PG 1351+640, showed no evidence of intrinsic reddening in any of the spectra obtained from the literature. In this case it is likely that the intrinsic reddening for this AGN truly is negligibly small. The Galactic reddening value was assumed for this object. For all other objects, the average reddening value in Table 3 was used, with the exception of NGC 5548. The value obtained from the simultaneously obtained UV and optical spectra was used in that case.

As well as uncertainties due to the observations (especially uncertainies caused by non-simultaneity), an additional uncertainty is introduced by the shape of the reddening curve. As mentioned above, a variety of reddening curves are seen for AGNs (see Gaskell et al. 2004). They all differ from the Galactic reddening curve in that they lack the λ 2175 extinction feature. Since we are not dealing with any lines near this dust feature, this has no effect on our results. The various reddening curves found for AGNs differ from one another (and from standard Galactic curves) primarily in the shape of the far UV spectrum (see Gaskell et al. 2004). Fortunately this only has a very small effect on our results because we are directly determining reddening over a wide wavelength range from the He II lines. The additional de-reddening uncertainties due to uncertainties in shape of the reddening curve are smaller than the uncertainties in determining the He II line ratio.

Fig. 1a,b shows the profiles of Lyα, C IV and C III] on the left-hand side and Ly α compared with the Hα and Hβ profiles on the right-hand side. In all case the profiles are shown after continuum subtraction, removal of contaminating lines, and application of a reddening correction using the Galactic reddening curve of Cardelli, Clayton & Mathis (1989).

4. Determining Conditions as a Function of Velocity

In paper 1 we presented grids, calculated from the photoionization code CLOUDY (Ferland 2002), of line ratios as a function of hydrogen number density (n_H) and ionization parameter (U). In Fig. 2 we show the emission-line ratios C III]/C IV and Lyα/C IV across the line profiles for the different AGNs. From this information one can determine n_H and U directly by comparing line ratios at a given velocity with the values predicted by photoionization models grids in paper 1.

Assuming, as is usually believed to be the case, that the broadening of broad emission lines is due to bulk motions of the emitting material, the displacement of emission in a line from the systemic velocity of the AGN is proportional *to the component of the velocity along the line of sight*, and not to the velocity itself. While emission in the high-velocity wing of a line must necessarily come from high-velocity gas, emission in the core of a line is not necessarily coming from low-velocity gas; some of it must be coming from high-velocity gas moving transverse to the line of sight.

In order to allow for the contribution of high-velocity gas to the cores of the lines, we assumed that the gas motions were isotropic. If gas clouds are moving isotropically and at the same speed, then the resulting emission line profile is a box car. The width of the box car depends on the bulk speed of the gas. For simplicity we arbitrarily divided line profiles into three line-emitting regions — a "very broad line region" (VBLR), a "broad-line region" (BLR), and an "intermediate-line region" (ILR) — and analyzed each zone separately[2].

[2]Note that we are not implying that the VBLR, BLR, and ILR are necessarily separate components. We are simply using them as labels for our arbitrary three zones. See the introduction to paper 1 for a discussion

Our procedure was as follows. First, the VBLR contribution was determined by the flux between 3000 and 5000 km s^{-1}. The boxcar due to this was subtracted off and then the "BLR" contribution was determined using the remaining flux between 1000 and 3000 km s^{-1}. Finally, this too was subtracted off and the ILR contribution remaining between 0 and 1000 km s^{-1} was determined. Since lines were generally not perfectly symmetric, we did the red and blue sides of each line separately (e.g., "BVBLR" for the blue side of the VBLR and "RVBLR" for the red side, etc.). Table 4 summarizes the velocity ranges assigned to the different line-emitting regions and we give an illustration of the regions in Fig. 3.

4.1. High-ionization Lines

The relative strengths of the high-ionization lines Lyα, C IV and C III] reveal the conditions in the gas close to the central engine of AGNs, (e.g., Davidson, 1977; Mushotzky & Ferland, 1984). Changes in a given line ratio as a function of velocity can be used as a probe of changes in the physical conditions in the gas of the BLR. We measured the line ratios for our five regions given in Table 4 for Lyα, C IV and C III], and determined the physical conditions corresponding to the average of the measured ratios determined from a grid of CLOUDY models shown in paper 1. In paper 1 we gave several arguments why even the high-velocity gas is optically thick. In the present paper we therefore only used the grids of optically-thick models. Although we have argued elsewhere (Snedden & Gaskell 1999) that abundances are probably several times solar in most AGNs, the model grids were calculated with solar abundances, since most other models in the literature assume solar abundances and, therefore, predicted conditions can be compared directly. The trends of how conditions vary across the profile are, of course, little affected by abundance. For reasons explained in Snedden & Gaskell (1999) the predicted n_H values are higher with enhanced abundances, but only by an offset. The relative change in conditions across the line profile is unaffected (see Fig. 2 of Snedden & Gaskell 1999 for an example of this).

The predicted physical conditions derived from each component of the high-ionization line profiles are plotted in Fig. 4. The uncertainties shown in the plots combine both the uncertainty from noise in the spectra and real variation in ratios across the emission-line zone. Therefore, trends across the profile could well be real, in spite of the overlap of the uncertainty bars. In Table 5 we give the velocity-averaged density and ionization parameter for each object. In Fig. 5 we show the average conditions for our components, normalized to the low-velocity component, for the sample as a whole. In Fig. 6 we show the mean ionizing

---

of the uses of these labels in the literature.

flux, $\Phi_H = U \cdot c \cdot n_H$, for our components, normalized to the low-velocity component.

4.2. Low-Ionization Lines

Although fully-ionized gas produces all the hydrogen lines, the Balmer lines are primarily produced in the optically-thick, warm, partially-ionized zone ("PIZ" – see Ferland 1999). The PIZ also produces strong emission from low-ionization lines such as Fe II, Mg II, and O I. As discussed in paper 1, the profiles of low-ionization lines (such as O I λ8446 and Mg II λ2798) are similar. Gaskell & Mariupolskaya (2001) find that, on average the FWHMs of Mg II and Hβ are the same, and detailed profile comparisons in individual objects support this (see Grandi 1980). O I λ8446 has a similar profile to Hα. Because of these similarities, we believe that conditions deduced from the Balmer lines refer to the PIZ where the low-ionization lines are produced.

As shown in paper 1, the Lyα/Hα and Hβ/Hα ratios can be used to determine physical conditions. In Fig. 7 we show the Hβ/Hα and Lyα/Hα ratios, as a function of velocity for the objects in our sample. We repeated the analysis described in the previous section to deduce conditions from Lyα/Hα and Hβ/Hα for our five arbitrary components. Although the line ratios show varying velocity dependencies from object to object, there is an overall trend. This is clear in Figs. 8 and 9 where we show the average Hβ/Hα and Lyα/Hα ratios for our sample. The error bars reflect the object-to-object variations.

We have not shown calculated physical conditions directly (as we did for the high-ionization lines) for two reasons. The first reason is the larger uncertainty in the de-reddened values for Lyα/Hα. The cause of this uncertainty is a combination of the lack of study of reddening indicators in individual objects, uncertainties in the appropriate reddening curve to use (see Gaskell et al. 2004), and the large range of wavelengths involved. The second reason is that the hydrogen line ratios are not yet as well determined in CLOUDY as are the line ratios for the high-ionization lines (see Ferland 1999). What we are able to do, in spite of the uncertainty in reddening and photoionization modeling, is look for *trends* in the physical conditions of the low-ionization gas as a function of velocity that are evidence of structure in the low-ionization gas. In Figs. 10 and 11 we therefore show the density and ionizing flux, averaged over the sample, and normalized to the low-velocity gas.

5. Results

5.1. High-Ionization Gas

In general, one can see from Figs. 4, 5 and 6 that there are no dramatic changes in predicted physical conditions between the ILR and BLR for most of the objects in our sample (although three objects do show statistically significant differences between the blue and red wings of the emission lines). The gas contributing to the ILR probably therefore has physical conditions similar to those of the gas that makes up the BLR. This suggests that the gas producing the ILR is not greatly different from the BLR-producing gas, and single-zone photoionization models may be justified, at least for the gas that produces the UV recombination lines.

Fig. 6 is especially important: there is no dependence of Φ_H on velocity. Since we know that Φ_H must be $\propto r^{1/4}$, the distance from the central source of ionizing radiation, Fig. 6 implies that *there is no correlation of v with r*. This is inconsistent with virialization of the gas producing the high-ionization lines, but consistent with the gas being radiatively accelerated.

5.2. Low-Ionization Gas

If we assume, as we have above, that at a given velocity all the lines are arising from a single component, the velocity-dependence of physical conditions deduced from the hydrogen lines contradict the velocity-dependencies deduced from the high-ionization lines. The hydrogen lines shown in Fig. 7 clearly display a trend towards higher ratios in the high-velocity gas, compared to the zero-velocity gas. This is true for both Lyα/Hα and Hβ/Hα, and is in agreement with the results of Shuder (1982, 1984), Crenshaw (1986) van Groningen (1987). Individual objects display a fair amount of variety in the shapes of the profiles (most notably PG 1351+640 – which, we have already noted, has problems with absorption lines). A major factor that could be influencing the object-to-object variation is the non-simultaneity of the UV and optical spectra. In some cases, we may be seeing residuals from incorrect de-blending, but this appears to be a secondary effect. Statistically, however, it is clear from Figs. 8 and 9 that the line ratios are higher in the wings.

The solution to the paradoxical behavior must be that there are two kinematically-distinct components to the BLR. It can be seen from Figs. 10 and 11 that both n_H and Φ_H increase in the high velocity gas relative to the low velocity gas. We see a decrease of about a factor of five in the zero-velocity gas relative to the high-velocity gas. The variation of Φ_H

with v is of particular interest, since it can tell us if the BLR gas is virialized. We compare the values at ± 2000 km s^{-1} and ± 4000 km s^{-1} to those predicted by the inverse-square law in Table 6. If we assume that the gas is gravitationally bound, and the ionizing photons come from a point source, then $v^2 \propto r^{-1}$, and $\Phi_H \propto r^{-2}$. Combining these relations, we get $(\Phi_{H1}/\Phi_{H2})^{1/4} = 2$ for the ratio of velocities in Table 6. Our results are completely consistent with this. It thus appears that the low-ionization line producing gas is completely or mostly virialized[3]. *This is fundamentally different than the results we obtained for the high-ionization gas.* There, Φ_H was found to be constant with v, within our measurement uncertainties.

6. Discussion

Evidence for the kinematics of the BLR has long been puzzling and contradictory. The blueshifting of the high-ionization lines (Gaskell 1982) argues for outflow of at least the high-ionization gas. The presence of intrinsic blueshifted broad and narrow absorption lines is unequivocal evidence that some outflow is taking place and the correlations between the FWHM of C IV and the minimum outflow velocity of broad absorption line (BAL) troughs (Lee & Turnshek 1995) is strong evidence for a connection between the kinematics of the BAL gas and the high-ionization BLR gas. On the other hand, there is strong evidence against outflow of the BLR. Cross-correlation of variations in the red and blue wings of C IV strongly rules out net radial motions (Gaskell 1987) and is instead completely consistent with virialization of the gas motions. The assumption of virialization of the gas motions has been the basis of reverberation mapping determinations of black hole masses. The dependence of line width on ionization is well known (see paper 1). Cross-correlation studies of AGN emission lines show that the higher ionization lines come from closer in (Gaskell & Sparke, 1986; Koratkar & Gaskell 1991; Krolik et al. 1991; Korista et al. 1995; Peterson & Wandel 2000; Onken & Peterson 2002). There is a good correlation between the line widths and the lag-determined distances from the central ionizing source for NGC 5548 (Peterson & Wandel 2000) and NGC 3783 (Onken & Peterson 2002).

In the context of gravity-dominated models, the constancy of the physical conditions with velocity for the high-ionization lines is unexpected. Most models of the BLR have assumed that n_H in BLR clouds is in some way dependent on distance from the central engine. This would reveal itself in the wings predicting different values for n_H and Φ than

[3]Korista & Goad (2004) are also able to reproduce the velocity-dependence of the Hα/Hβ ratio in NGC 5548 with a virialized model.

the cores of emission lines. Based on the high-ionization lines, we see no evidence of this for most of our objects.

If the BLR is spatially extended, then Φ_H should change with position and presumably, velocity. As is obvious from Fig. 6, we do not see this. Having the velocity be independent of position is instead consistent with the gas forming a wind at terminal velocity, or being confined by that wind. The wind must be radially symmetric to a large degree to produce the symmetrical profiles that are observed.

Gaskell (1987) and Collin-Souffrin & Lasota (1988) argue, on the basis of profile differences and photoionization-modelling issues, for a two-component BLR: one component with a classical nebular spectrum and the other with a strong PIZ. The case for such a two-component model is summarized in Gaskell (2000). We believe that a similar two-component model is necessary to reconcile the conflicting sets of evidence for radial outflow of the BLR versus virialization. The evidence presented here supports such a picture: the unexpected velocity independence of physical conditions in the high-ionization gas cannot arise when the gas motions are due to gravity, while the velocity dependence of the conditions in the low-ionization gas is completely consistent with gravity domination of the motion.

While we have, for simplicity, assumed that the motions of both BLR components are isotropic (and therefore probably spherically symmetric), the motions of the low-ionization gas could well be in a disk. For NGC 5548 the transfer function (the function with which the continuum light curve is convolved to produce a line light curve) for the high-ionization gas (see, for example, Krolik et al. 1991) is consistent with a spherically-symmetric distribution of gas, while the transfer function for Hβ (Horne, Welsh, & Peterson 1991) is not. The Hβ transfer function is, instead, compatible with a disk structure. Some AGNs (3C 390.3 objects) show very obvious disk-like Balmer line profiles and we have argued elsewhere (Gaskell & Snedden 1999) that the Balmer line profiles in all AGNs are compatible with all AGNs having a significant disk contribution. Disk-plus-wind models have long been considered for the origin of AGN emission line regions (e.g., Shields 1977, Collin-Souffrin et al. 1980, Chiang & Murray 1996, Bottorff et al. 1997). We believe that our results support this picture[4]. Our sample here does not include an AGN with a very broad disk component. In a study of the proto-typical disk emitter, 3C 390.3, Nazarova, Bochkarev, & Gaskell (2004) find that Lyα/Hβ is higher in the *core* of the lines. This is consistent with the much greater width of the disk component in 3C 390.3.

We have shown above that the assumption of a single kinematic component produces

[4]van Groningen (1987) reached a similar conclusion from consideration of the Balmer lines alone in Mrk 335.

contradictory results when the high- and low-ionization lines are used to deduce the velocity dependence of physical conditions. While we have shown that there is a need for two components, separating out emission from a disk and a wind component is very difficult. A more thorough analysis needs to recognize that there must be some contribution of the high-ionization gas to the Balmer lines, and there must also be some contribution of the low-ionization gas to the profile of Lyman α[5]. The velocity independence of conditions deduced from the strong UV lines suggests that there is little contribution to Lyman α from the low-ionization gas, as Collin-Souffrin, Dumont, & Tully (1982) have suggested should be the case. When improved models for hydrogen emission become available and reliable reddening estimates, one should ideally calculate and subtract off the high-ionization contribution to the Balmer lines. Because of the limitations of models of hydrogen emission, our determination of conditions from the hydrogen lines is the weakest part of our analysis. The assumption of a single model obviously overestimates the Ly α coming from the low-ionization lines because of the strong contribution from the high-ionization lines. This will systematically change the zero points of our estimates of physical conditions.

7. Conclusions

Our photoionization analysis of the change of line ratios with velocity in a sample of AGNs shows that conditions deduced from the high-ionization lines are surprisingly independent of velocity, while conditions deduced from the hydrogen lines alone show a strong velocity dependence. We suggest that the resolution to this paradox is that the high- and low-ionization lines are arising from predominantly different gas. The behavior of the high-ionization lines is consistent with them arising from a radiatively-driven outflow, while the behavior of the Balmer lines is consistent with them arising from gravitationally-bound gas. These results are consistent with disk-plus-wind models.

We do not find any evidence for a distinct "intermediate-line region".

We are grateful to Giovanna Stirpe for making her optical spectra available in machine-readable format. We also wish to thank Mike Harvanek and Bev Wills for helpful comments on this work. MG wishes to acknowledge the hospitality of Apache Point Observatory where this work was completed. This work has been supported in part by grant AR-05796.01-94A from the Space Telescope Science Institute, which is operated by AURA, Inc., under NASA contract NAS5-26555.

---

[5]Note that we used Lyman α in both the high- and low-ionization line analyses.

REFERENCES

Baldwin, J. A. & Netzer, H. 1978, ApJ, 226, 1

Bechtold, J., Czerny, B. et al. 1987, ApJ, 314, 699

Boroson, T. A. & Green, R. F. 1992, ApJS, 80, 109

Bottorff, M. C., Korista, K. T., Shlosman, I, Blandford, R. D. 1997, ApJ, 479, 200

Brotherton, M. S., Wills, B. J., Francis, P. J. & Steidel, C., C. 1994, ApJ, 430, 495

Cardelli, J. A., Clayton, G. C. & Mathis, J. S. 1989, ApJ, 345, 245

Chiang, J. & Murray, N. 1996, ApJ, 466, 704

Collin-Souffrin, S. Dumont, S., Tully, J. 1982, A&A, 106, 362

Collin-Souffrin, S., Joly, M., Dumont, S., & Heidmann, N. 1980, A&A, 83, 190

Collin-Souffrin, S. & Lasota, J.-P. 1988, PASP, 100, 1041

Corbin, M. R. & Boroson, T. A. 1996, ApJS, 107, 69

Crenshaw, D. M. 1986, ApJS, 62, 821

Davidson, K. 1972, ApJ, 171, 213

Davidson, K. 1977, ApJ, 218, 20

Dietrich, M. et al. 1993, ApJ, 408, 416

Ferland, G. J. 1999, in *Quasars and Cosmology*, ASP Conference Series 162, ed. G. J. Ferland & J. A. Baldwin (San Francisco: Astron. Soc. Pacific), 147

Ferland, G. J. 2002, *Hazy, a Brief Introduction to Cloudy*, U.Kentucky Dept. of Physics & Astronomy Internal Report

Gaskell, C. M. 1982, ApJ, 263, 79

Gaskell, C. M. 1987, in *Astrophysical Jets and Their Engines*, ed. W. Kundt (Dordrecht: Reidel), p. 21

Gaskell, C. M. 2000, New Astr. Rev., 44, 563

Gaskell, C. M., Goosmann, R. W., Antonucci, R. R. J., & Whysong, D. H. 2004, ApJ submitted (astro-phy/0309595)

Gaskell, C. M. & Mariupolskaya, V. Y. 2001 in *Mass Outflow in Active Galactic Nuclei: New Perspectives*, ASP Conf. Ser. 255, ed. D. M. Crenshaw, S. B. Kraemer, & I. M. George (San Francisco: Ast. Soc. Pacific), 261

Gaskell, C. M. & Snedden, S. A. 1999, in ASP Conf. Ser. 175, Structure and Kinematics of Quasar Broad Line Regions, ed. C. M. Gaskell, W. N. Brandt, M. Dietrich, D. Dultzin-Hacyan, & M. Eracleous (San Francisco: Astron. Soc. Pacific), 157

Gaskell, C. M. & Sparke, L. S. 1986, ApJ, 305, 175

Grandi, S. A. 1980, ApJ, 238, 10

Horne, K., Welsh, W. F., & Peterson, B. M. 1991, ApJ, 367, L5

Koratkar, A. P. & Gaskell, C. M. 1991, ApJS, 75, 719

Korista, K. T. et al. 1995, ApJS, 97, 285

Korista, K. T., and Goad, M. 2004, ApJ in press (astro-ph/0402506)

Krolik, J. H., Horne, K., Kallman, T. R., Malkan, M. A., Edelson, R. A. & Kriss, G. A. 1991, ApJ, 371, 541

Kwan, J. & Krolik, J. H. 1979, ApJL, 233, 91

Lee, L. W. & Turnshek, D. A. 1995, ApJL, 453, 61

MacAlpine, G. M. 1974, ApJ, 193, 37

Marziani, P., Sulentic, J. W., Dultzin-Hacyan, D., Calvani, M. & Moles, M. 1996, ApJS, 104, 37

Mushotzky, R. F. & Ferland, G. J. 1984 ApJ, 278, 558

Nazarova, L. S., Bochkarev, N. G., & Gaskell, C. M. 2004, Ast. Ap. Trans., in press.

Onken, C. A. & Peterson, B. M. 2002, ApJ, 572, 746

Peterson, B. M. & Wandel, A. 2000, ApJ, 540, L13

Seaton, M. J. 1978, MNRAS, 185, P5

Seaton, M. J. 1979, MNRAS, 187, P73

Shields, G. A. 1977, ApL, 18, 119

Shuder, J. M. 1982, ApJ, 259, 48

Shuder, J. M. 1984, ApJ, 280, 491

Snedden, S. A. & Gaskell, C. M. 1999, ApJ, 512, L91

Snedden, S. A. & Gaskell, C. M. 2004, ApJ submitted (Paper 1) (astro-ph/0402508)

Stirpe, G. M. 1991, A&A, 247, 3

Stirpe, G. M. 1990, A&AS 85, 1049

van Groningen, E. 1987, A&A, 186, 103

Ward, M. J. & Morris, S. L. 1984, MNRAS, 207, 867

Wills, B. J., Thompson, K. L., Han, M., Netzer, H., Wills, D., Baldwin, J. A., Ferland, G. J., Browne, I. W. A. & Brotherton, M. S. 1995, ApJ, 447, 139

Winge, C., Pastoriza, M. G. et al. 1992, ApJ, 393, 98

Winge, C., Peterson, B. M., et al. 1996, ApJ, 469, 648

Object	α	F_{1000}
B2 2201+31A	0.640	1.38
Fairall 9	1.48	4.60
NGC 3783	1.54	9.25
NGC 5548 (low)	0.965	3.34
NGC 5548 (high)	1.12	5.49
PG 1116+215	1.35	6.30
PG 1211+143	1.12	3.55
PG 1351+640	0.628	2.27
Pks 2251+113	0.482	0.506

Table 1: The power-law continuum parameters. α is the power-law index. F_{1000} is the flux at 1000 Å$\cdot 10^{-14} \cdot erg \cdot s^{-1} \cdot cm^{-2} \cdot$ Å^{-1} .

	A_V								
Object	(1)	(2)	(3)	(4)	(5)	(6)	(7)	(8)	(9)
B2 2201+31A	1.26	(0.047)	···	···	···	···	···	0.085	···
Fairall 9	0.71	(0.043)	···	···	0.13	···	···	(0.043)	···
NGC 3783	···	0.86	1.00	···	···	0.27	···	1.44	···
NGC 5548	···	0.28	···	···	···	···	···	0.033	1.08
PG 1116+215	(0.037)	(0.037)	···	···	···	···	0.58	1.68	···
PG 1211+143	(0.11)	(0.11)	···	0.31	···	···	0.20	0.97	···
PG 1351+640	(0.043)	(0.043)	···	···	···	···	(0.043)	(0.043)	···
Pks 2251+113	(0.198)	(0.198)	···	···	···	···	(0.198)	0.58	···

Table 2: Galactic Plus Intrinsic Reddening. Reddening was calculated from He II λ1640 and λ4684 fluxes. A table of Galactic reddenings for our objects can be found in Table 3.?. In cases where there was no indication of intrinsic reddening, the galactic value was assumed (parentheses). The various sources for the He IIfluxes are: (1) Corbin & Boroson (1996) (2) Marziani et al. (1996) (3) Ward & Morris (1984) (4) Bechtold et al. (1987) (5) Winge et al. (1996) (6) Winge et al. (1992) (7) Boroson & Green (1992) (8) Stirpe (1990), Wills et al. (1995), Marziani et al. (1996) (9) Dietrich et al. (1993), Korista et al. (1995).

Object	Minimum A_V	Average A_V	Maximum A_V
B2 2201+31A	0.047	0.464	1.26
Fairall 9	0.043	0.230	0.710
NGC 3783	0.372	0.890	1.44
NGC 5548	0.034	0.464	1.08
PG 1116+215	0.037	0.584	1.68
PG 1211+143	0.105	0.338	0.970
PG 1351+640	0.043	...	...
Pks 2251+113	0.198	0.294	0.58

Table 3: Range of reddenings for the sample. In our analysis the average reddening was assumed for all objects in the sample, except for PG 1351+640, which appears to have negligible intrinsic reddening. Galactic reddening was assumed for this object.

Region	Velocity Range (km s^{-1})
BVBLR	-5000 to -3000
BBLR	-3000 to -1000
ILR	-1000 to 1000
RBLR	1000 to 3000
RVBLR	3000 to 5000

Table 4: The different line-emitting regions and their associated projected velocities. Note that the blue side of the so-called Very-Broad-Line region (VBLR) is denoted “BVBLR”, the red side as “RVBLR” and so forth.

Object	log U	log n_H
B2 2201+31A	-1.63	9.30
Fairall 9	-1.30	10.29
NGC 3783	-1.38	10.45
NGC 5548 (low)	-1.16	10.21
NGC 5548 (high)	-1.31	10.49
PG 1116+215	-1.88	10.24
PG 1211+143	-1.78	10.52
PG 1351+640	-1.61	9.77
Pks 2251+113	-1.49	9.82

Table 5: The predicted physical conditions in the BLR based on the high-ionization lines. The photoionization model grid assumed 1$Z_\odot$ abundances. The two entries for NGC 5548 are for the low and high activity states during the *International AGN Watch* monitoring campaign.

v_1/v_2	$(\Phi_{H1}/\Phi_{H2})^{1/4}$
-4000/-2000	1.73 (+0.51, -0.67)
4000/2000	1.88 (+0.49, -0.05)

Table 6: A check of how well Φ_H conforms to the values expected from the inverse-square law. For the ratio of velocities in the table, one would expect $(\Phi_{H1}/\Phi_{H2})^{1/4} = 2$ if the inverse-square law is obeyed.

Fig. 1.— *a)* The major emission line profiles of the sample. Lyα is shown in both columns as a solid line. The left-hand column also shows C IV as a dashed line and C III] as a dotted line. The right-hand column shows Hα as a dashed line and Hβ as a dotted line. *b)* The major emission line profiles (cont.).

Fig. 2.— *a)* The high-ionization line ratios. The left-hand column shows C III]/C IV as a function of projected Doppler velocity across the line profile. The right-hand column shows the same for Lyα/C IV. *b)* The high-ionization line ratios (cont.).

Fig. 3.— An illustration of the arbitrary line-emitting regions used for the analysis in this paper. The nomenclature is described in Table 4.

Fig. 4.— The ionization parameter, U, (circles) and hydrogen density, n_H, (triangles) as a function of line-emitting region, based on the high-ionization lines. The values of U and n_H were determined from the line ratios using the CLOUDY photoionization model grids described in paper 1.

Fig. 5.— The hydrogen density, n_H, as deduced from the high-ionization lines, as a function of line-emitting region, averaged over our sample and normalized to the ILR.

Fig. 6.— The ionizing photon flux, Φ_H, as deduced from the high-ionization lines, as a function of line-emitting region, averaged over our sample and normalized to the ILR.

Fig. 7.— *a)* The low-ionization line ratios. The left-hand column shows Hβ/Hα as a function of projected Doppler velocity across the line profile. The right-hand column shows the same for Lyα/Hα. *b)* The low-ionization line ratios (cont.).

Fig. 8.— The Balmer decrement as a function of projected Doppler velocity, averaged over our sample.

Fig. 9.— Lyα/Hα as a function of projected Doppler velocity, averaged over our sample.

Fig. 10.— The hydrogen density, n_H, as deduced from the low-ionization lines, as a function of line-emitting region, averaged over our sample and normalized to the ILR.

Fig. 11.— The ionizing photon flux, Φ_H, as deduced from the low-ionization lines, as a function of the line-emitting region, averaged over our sample and normalized to the ILR.

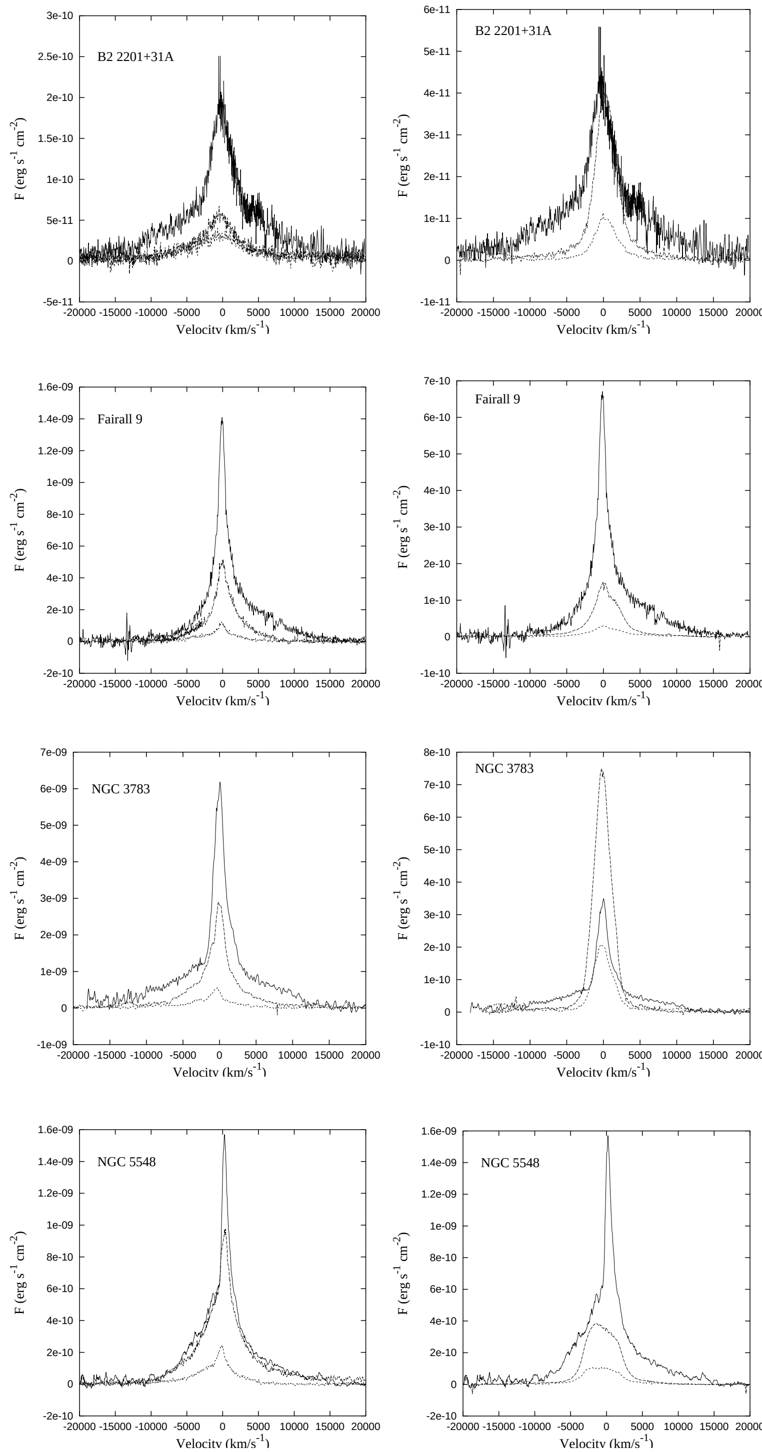
B2 2201+31A
B2 2201+31A
Fairall 9
Fairall 9
NGC 3783
NGC 3783
NGC 5548
NGC 5548
F (erg s^{-1} cm^{-2})
Velocity (km/s^{-1})

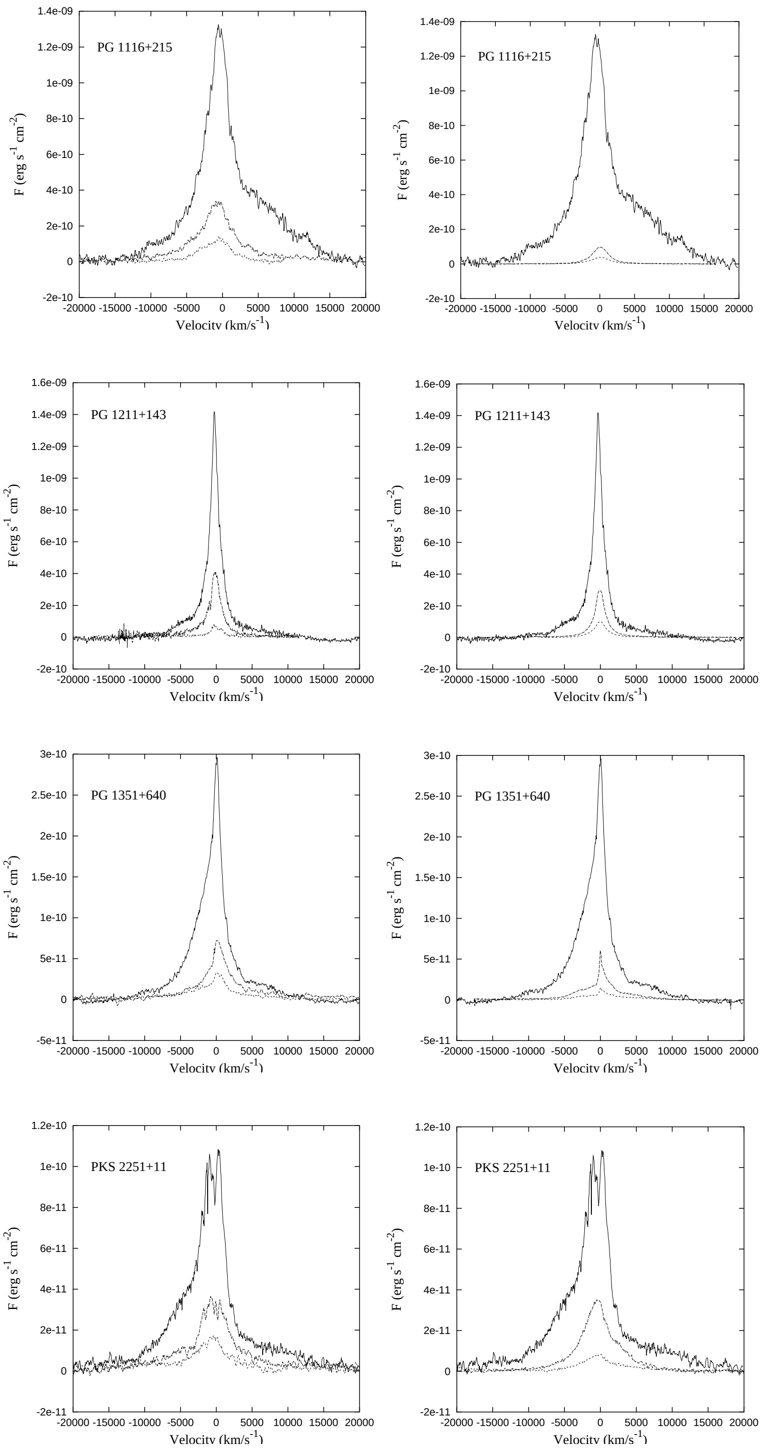
PG 1116+215
PG 1116+215
PG 1211+143
PG 1211+143
PG 1351+640
PG 1351+640
PKS 2251+11
PKS 2251+11
F (erg s^{-1} cm^{-2})
Velocity (km/s^{-1})

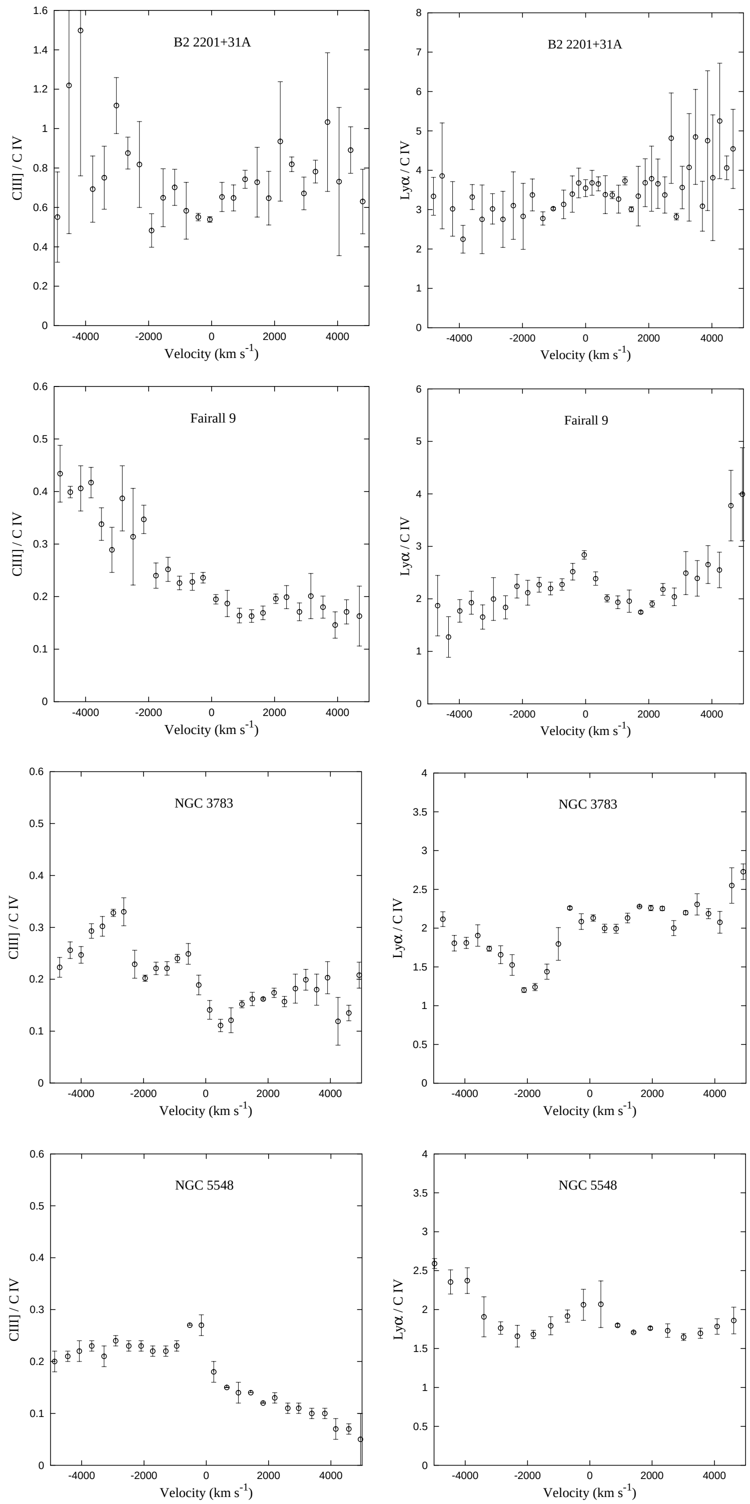
B2 2201+31A
CIII] / C IV
Velocity (km s-1)
B2 2201+31A
Lyα / C IV
Velocity (km s-1)
Fairall 9
CIII] / C IV
Velocity (km s-1)
Fairall 9
Lyα / C IV
Velocity (km s-1)
NGC 3783
CIII] / C IV
Velocity (km s-1)
NGC 3783
Lyα / C IV
Velocity (km s-1)
NGC 5548
CIII] / C IV
Velocity (km s-1)
NGC 5548
Lyα / C IV
Velocity (km s-1)

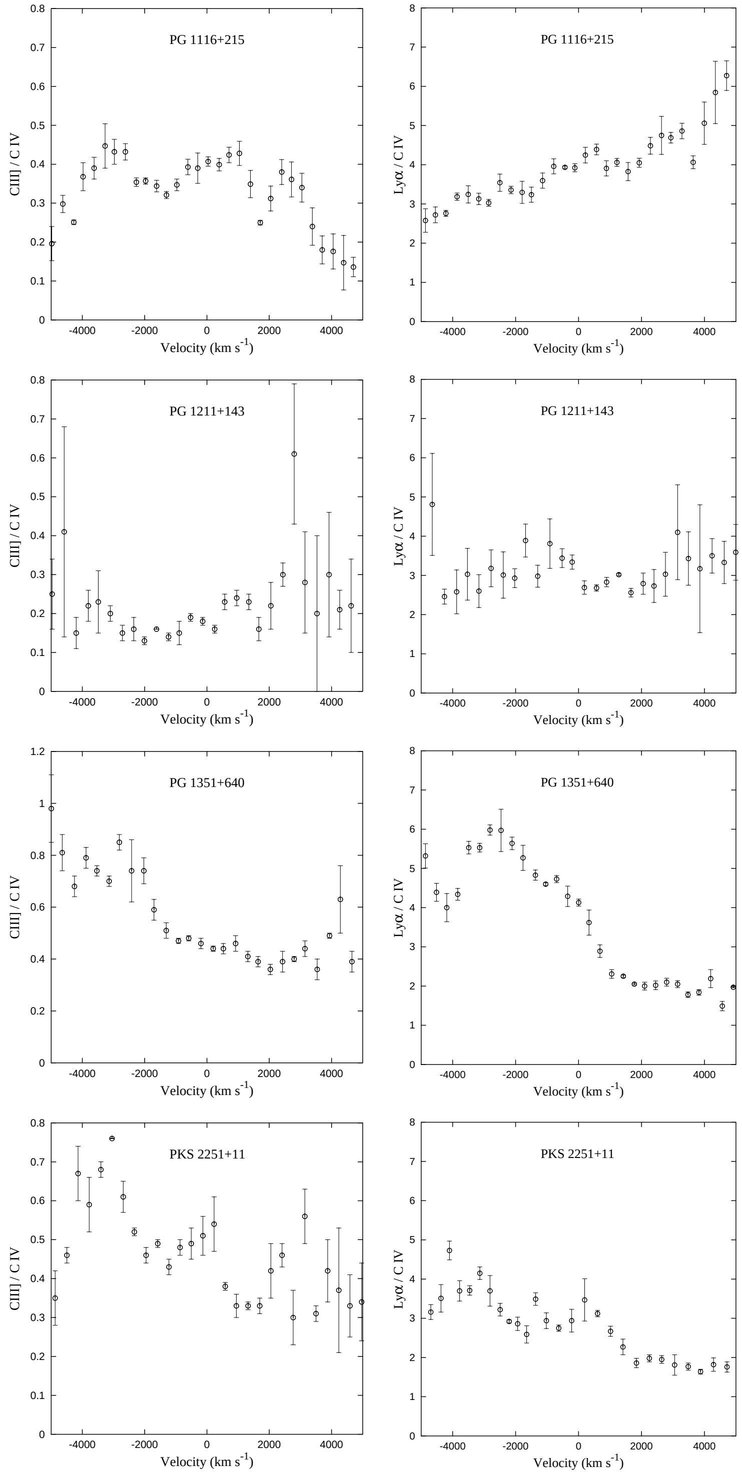
PG 1116+215
CIII] / C IV
Lyα / C IV
PG 1211+143
PG 1351+640
PKS 2251+11
Velocity (km s-1)

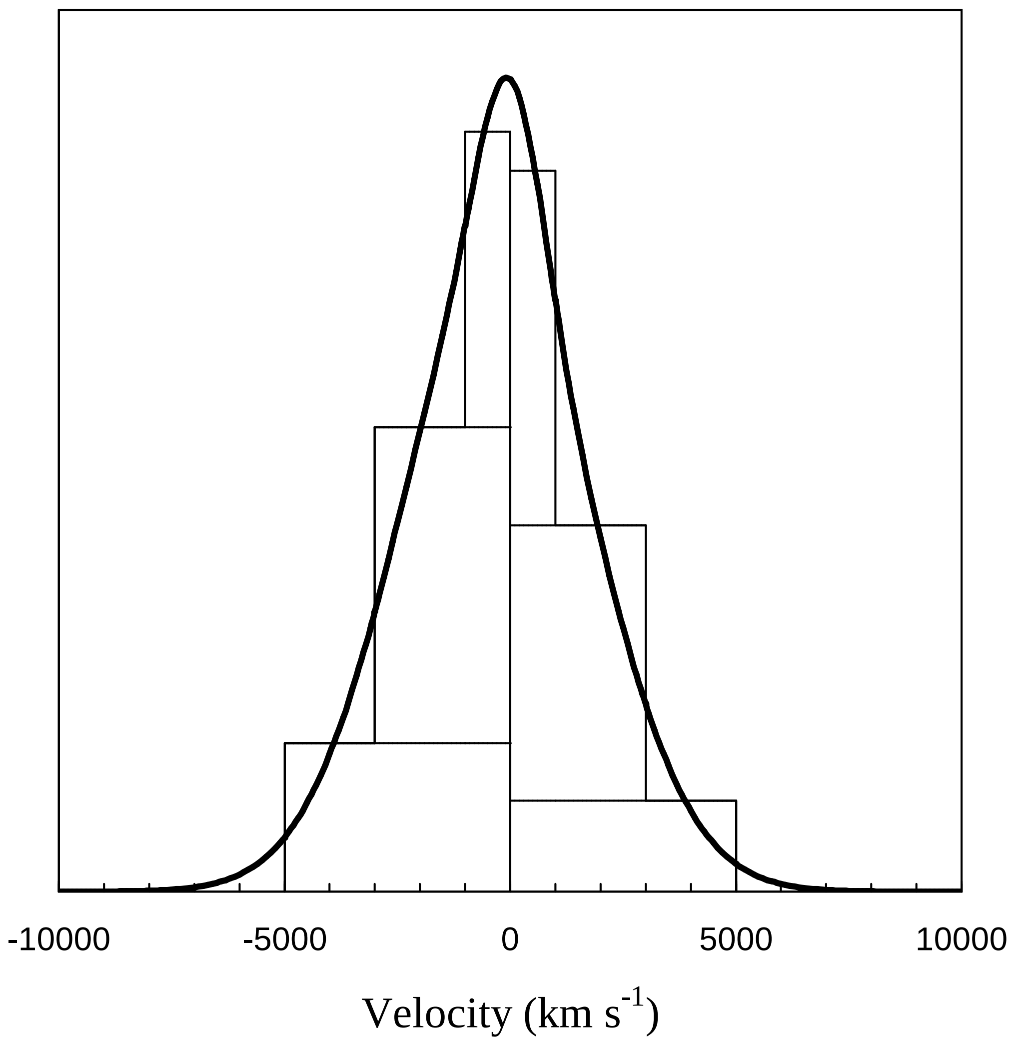
-10000
-5000
0
5000
10000
Velocity (km s-1)

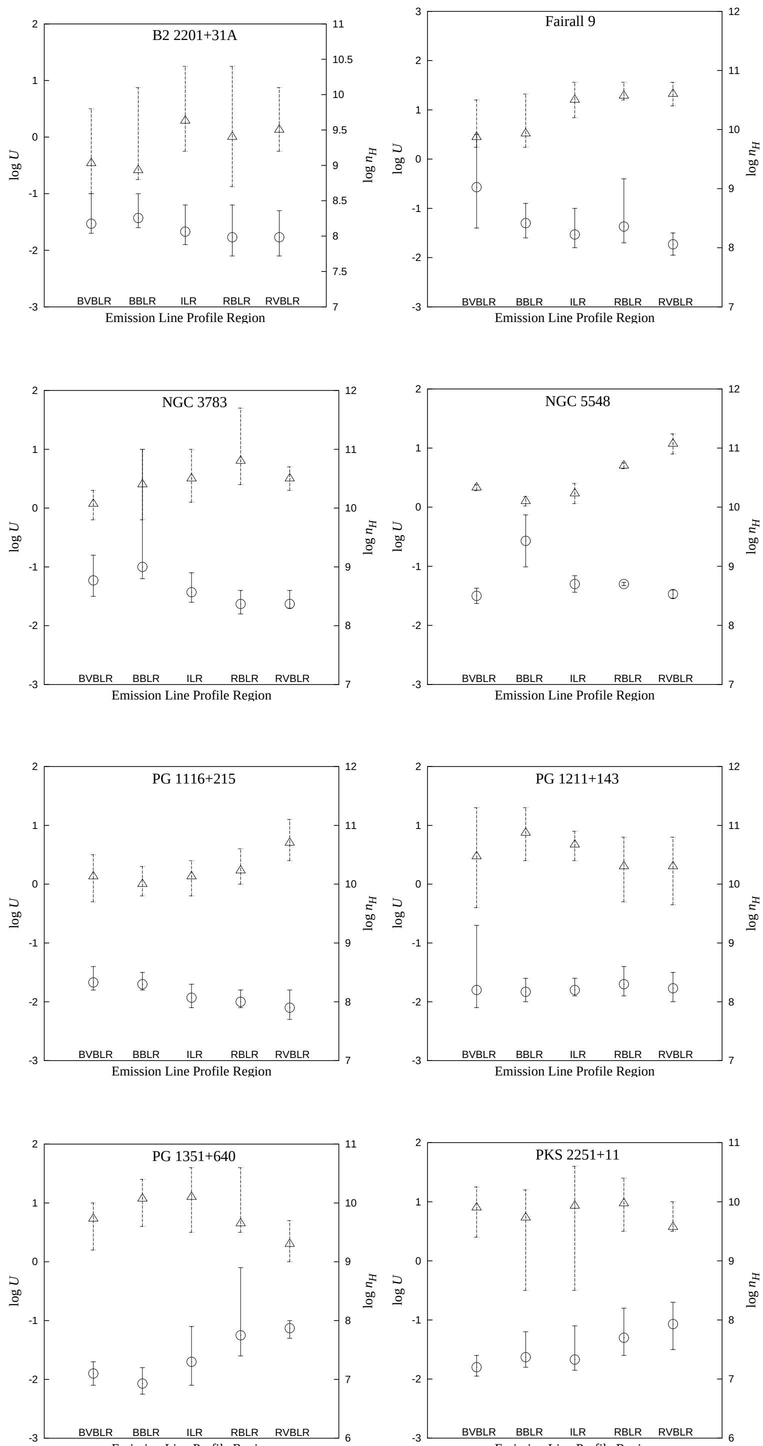
B2 2201+31A
Fairall 9
NGC 3783
NGC 5548
PG 1116+215
PG 1211+143
PG 1351+640
PKS 2251+11
log U
log n_H
BVBLR
BBLR
ILR
RBLR
RVBLR
Emission Line Profile Region

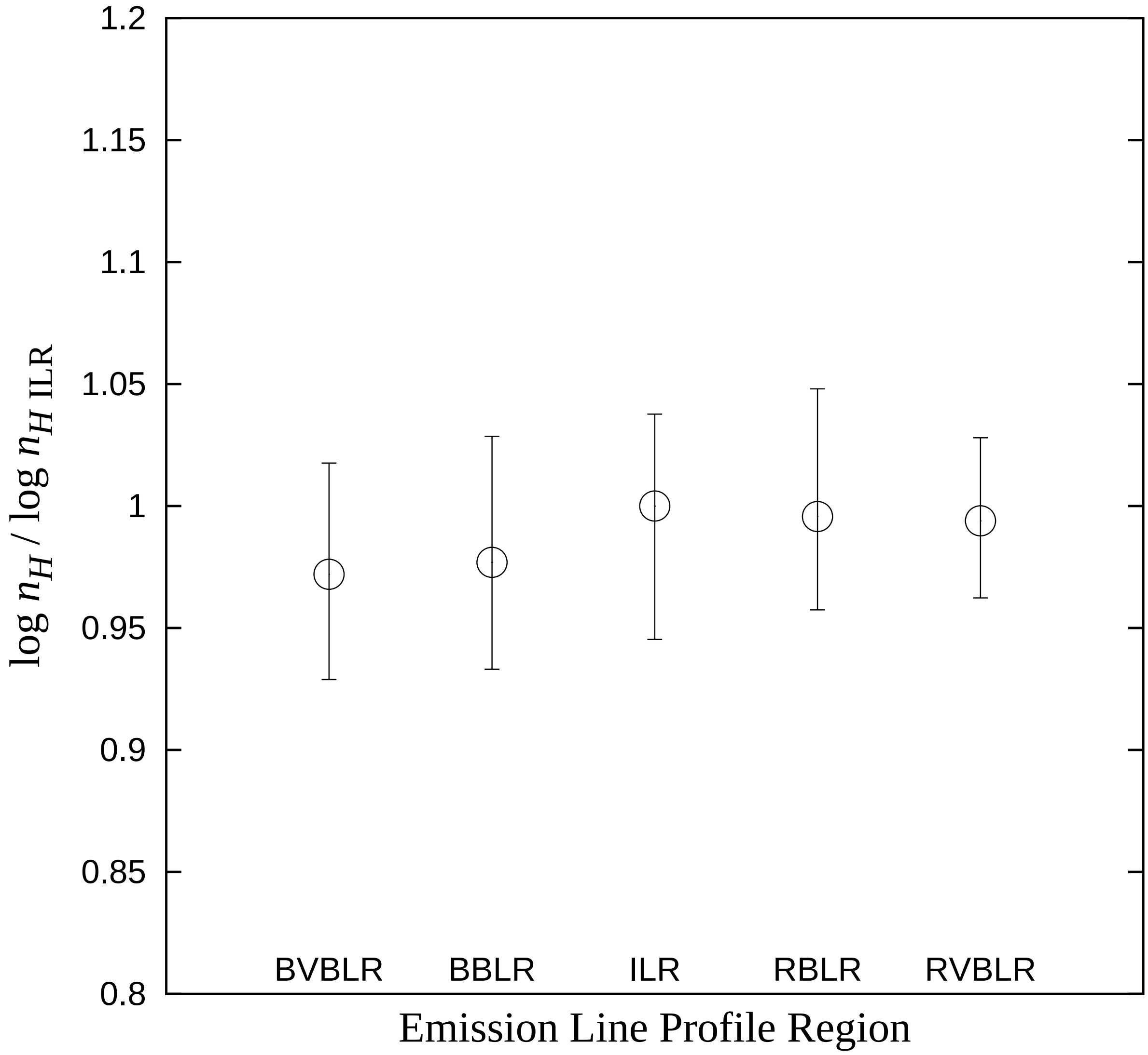
1.2
1.15
1.1
1.05
1
0.95
0.9
0.85
0.8
log n_H / log $n_{H\ \mathrm{ILR}}$
BVBLR
BBLR
ILR
RBLR
RVBLR
Emission Line Profile Region

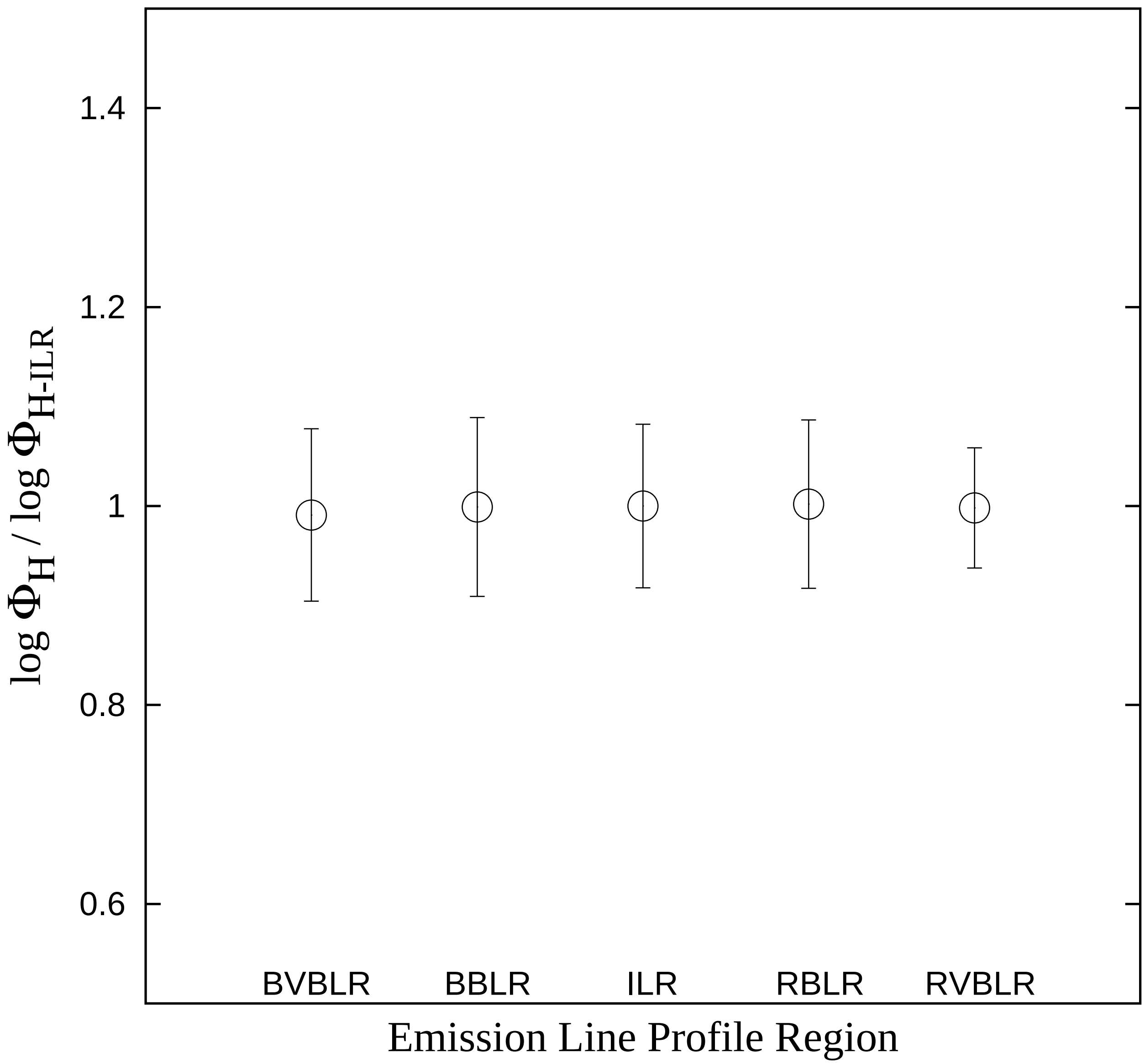
1.4
1.2
1
0.8
0.6
log Φ_H / log Φ_H-ILR
BVBLR
BBLR
ILR
RBLR
RVBLR
Emission Line Profile Region

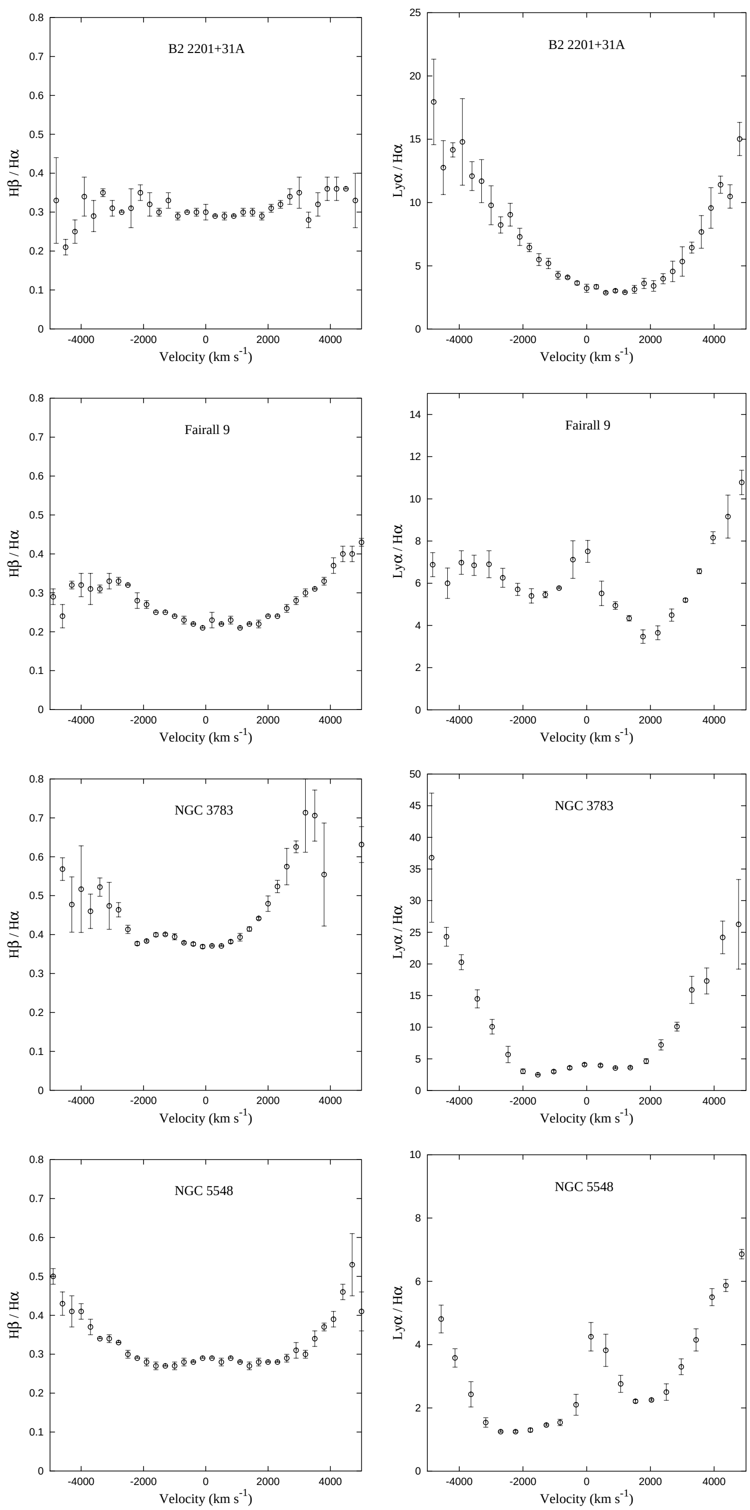
B2 2201+31A
Hβ / Hα
Velocity (km s-1)
B2 2201+31A
Lyα / Hα
Velocity (km s-1)
Fairall 9
Hβ / Hα
Velocity (km s-1)
Fairall 9
Lyα / Hα
Velocity (km s-1)
NGC 3783
Hβ / Hα
Velocity (km s-1)
NGC 3783
Lyα / Hα
Velocity (km s-1)
NGC 5548
Hβ / Hα
Velocity (km s-1)
NGC 5548
Lyα / Hα
Velocity (km s-1)

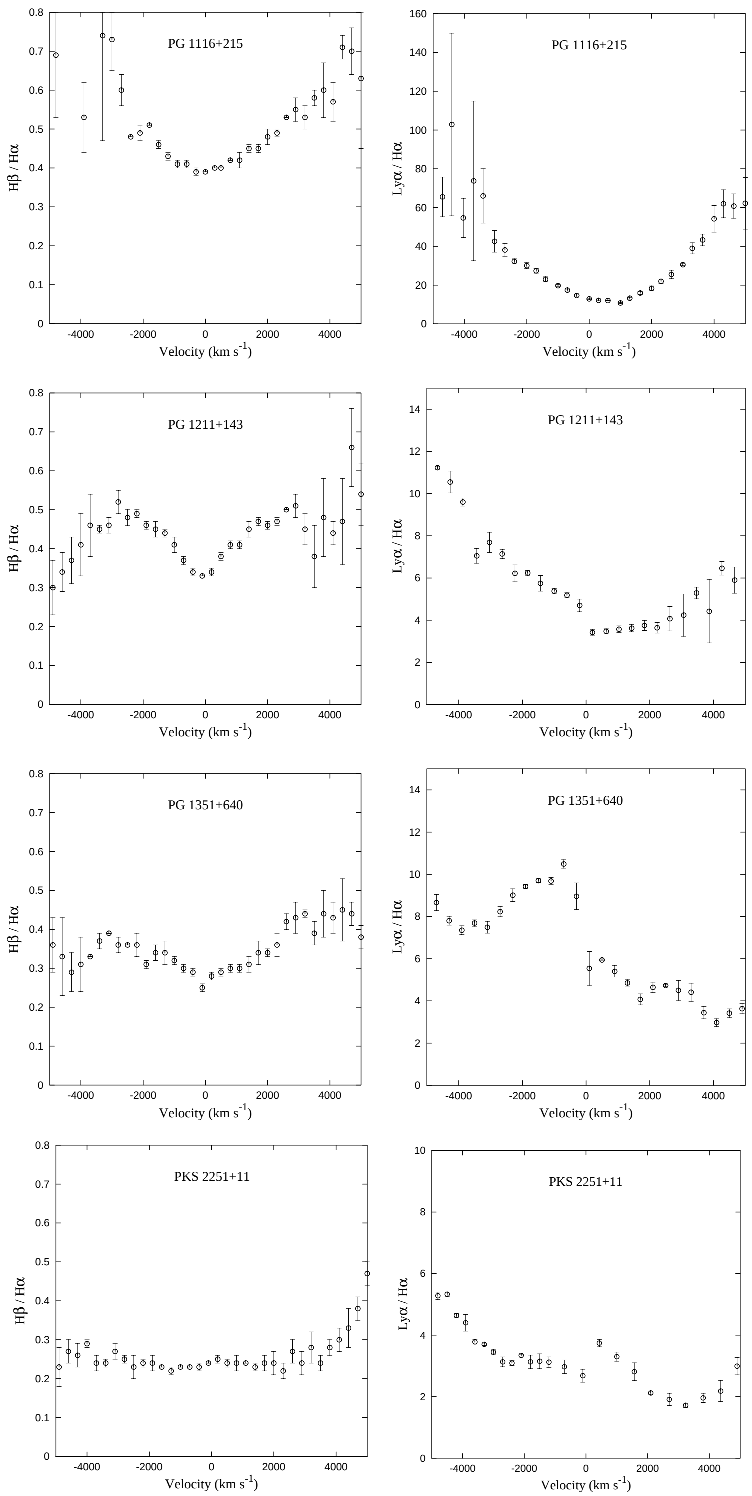
PG 1116+215
Hβ / Hα
Velocity (km s-1)
PG 1116+215
Lyα / Hα
Velocity (km s-1)
PG 1211+143
Hβ / Hα
Velocity (km s-1)
PG 1211+143
Lyα / Hα
Velocity (km s-1)
PG 1351+640
Hβ / Hα
Velocity (km s-1)
PG 1351+640
Lyα / Hα
Velocity (km s-1)
PKS 2251+11
Hβ / Hα
Velocity (km s-1)
PKS 2251+11
Lyα / Hα
Velocity (km s-1)

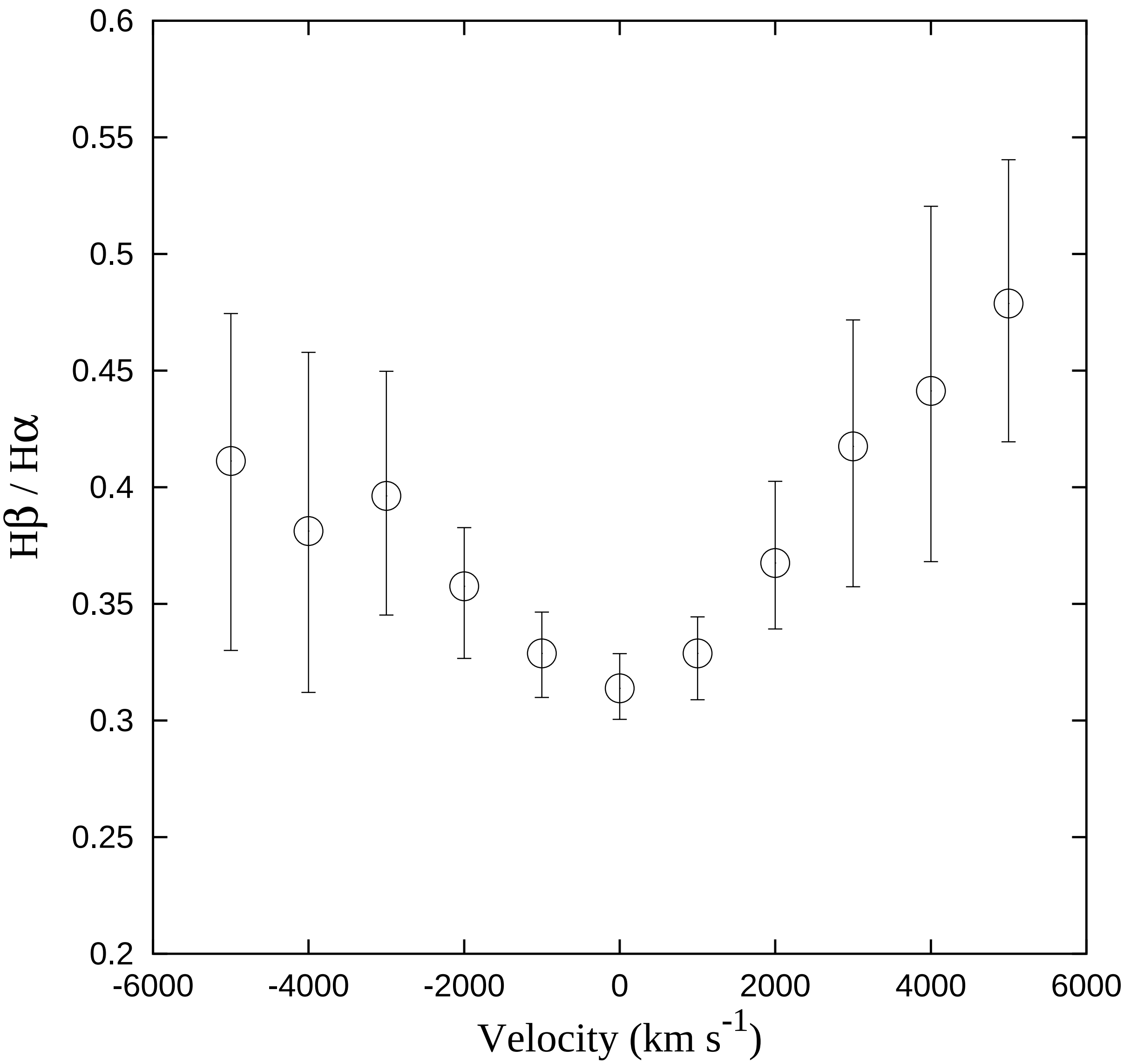
Hβ / Hα
0.6
0.55
0.5
0.45
0.4
0.35
0.3
0.25
0.2
-6000
-4000
-2000
0
2000
4000
6000
Velocity (km s-1)

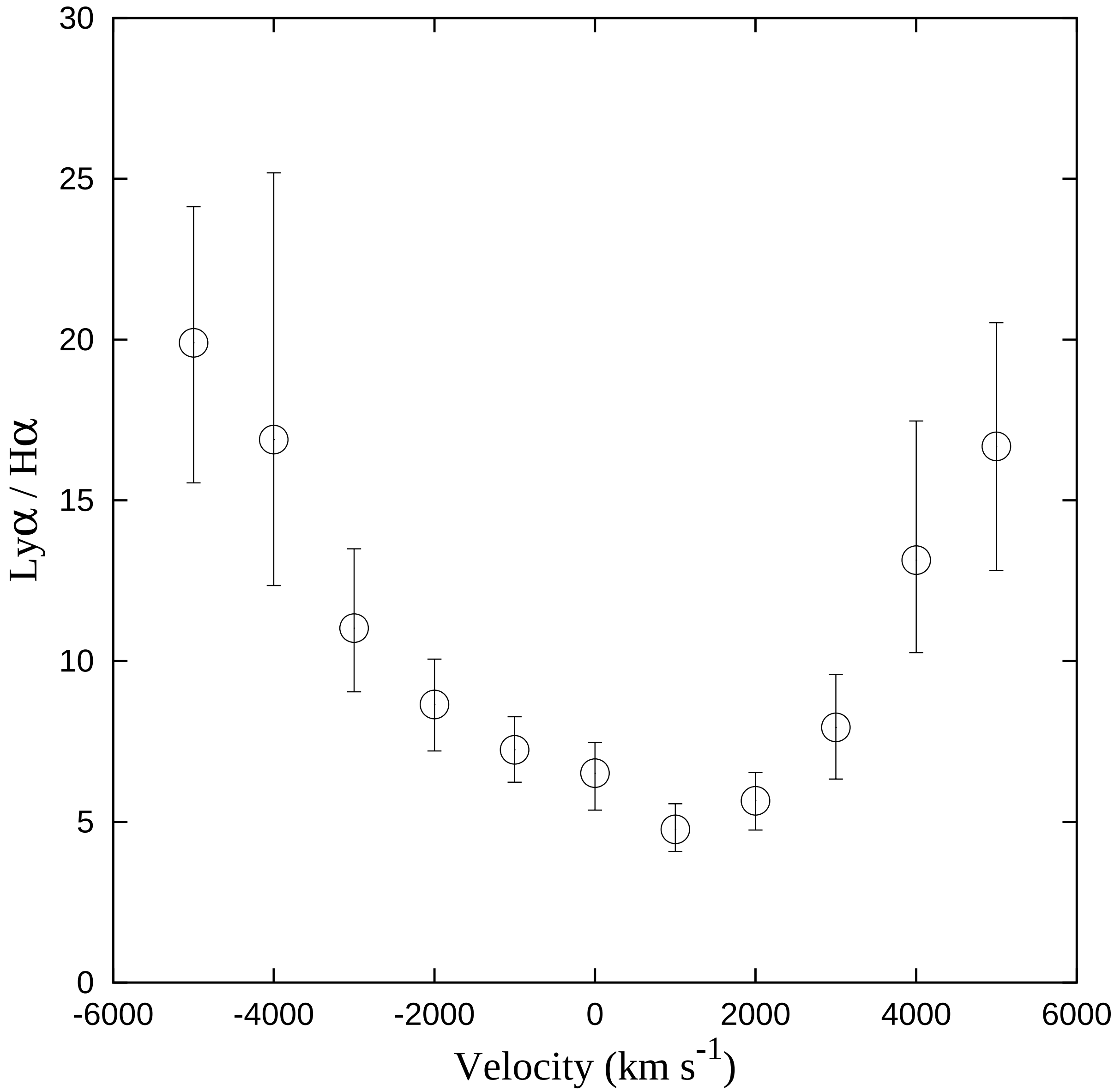

Lyα / Hα
Velocity (km s-1)
0
5
10
15
20
25
30
-6000
-4000
-2000
0
2000
4000
6000

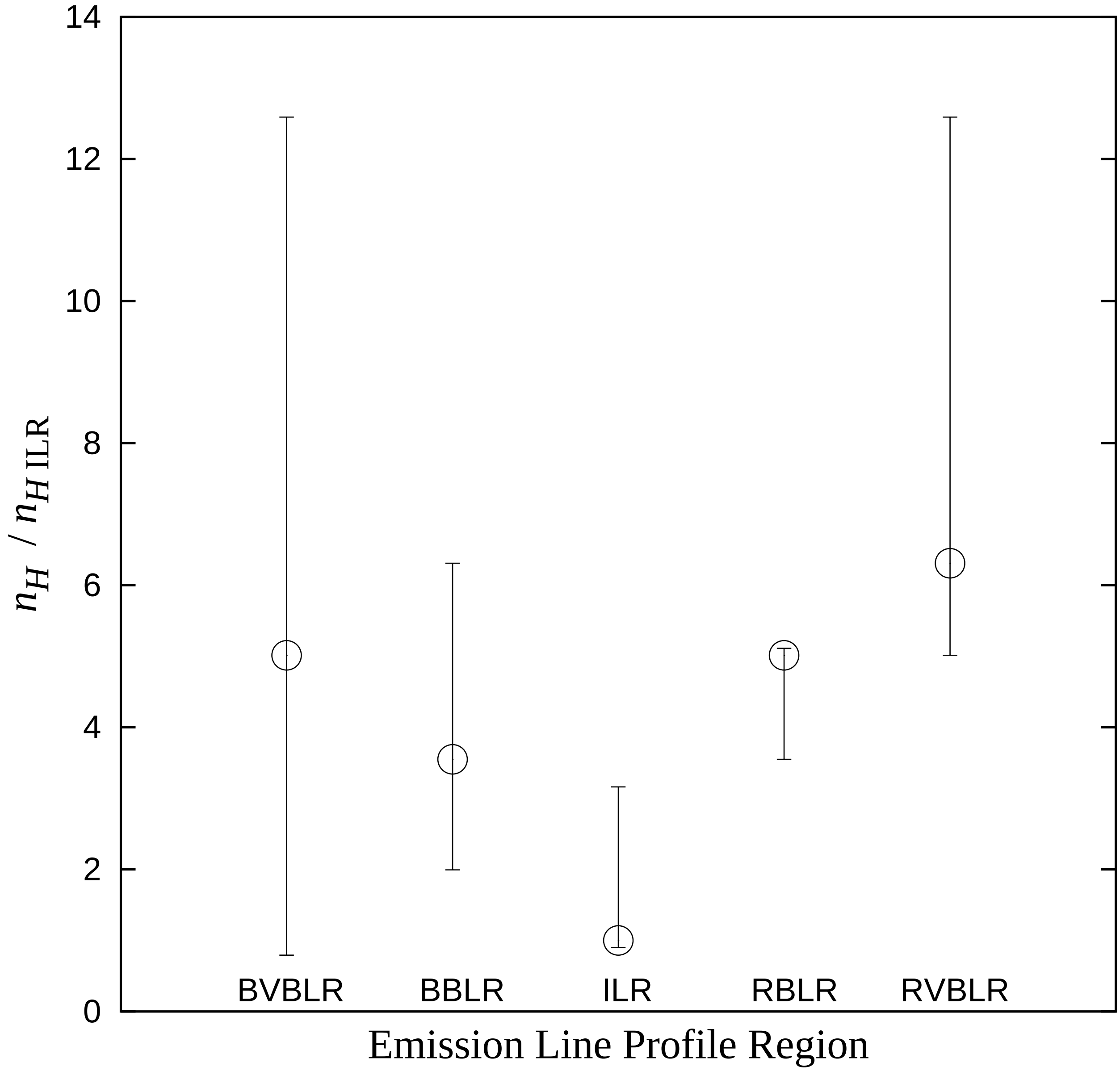
14
12
10
8
6
4
2
0
n_H / $n_{H\,\mathrm{ILR}}$
BVBLR
BBLR
ILR
RBLR
RVBLR
Emission Line Profile Region

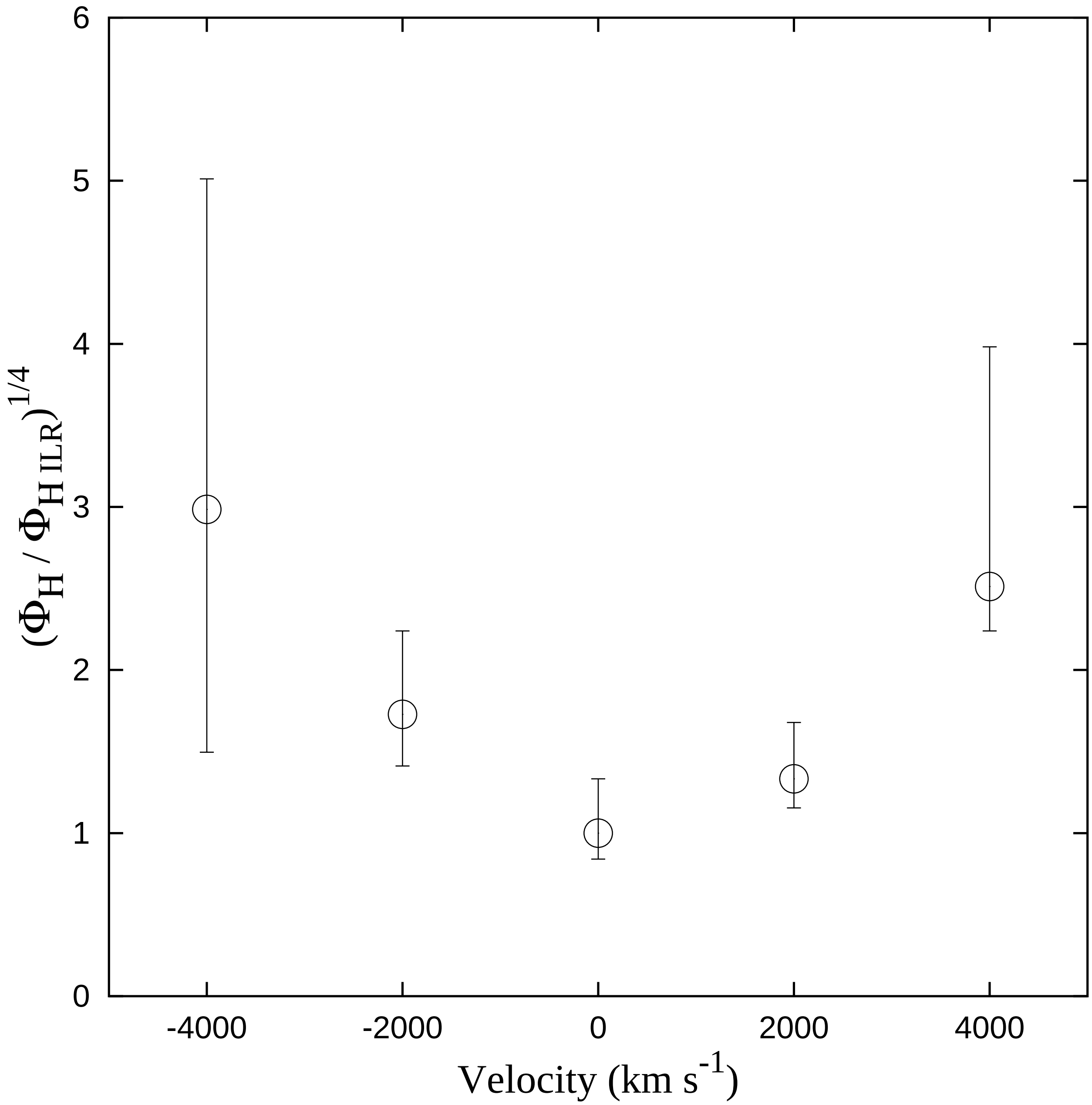

$(\Phi_H / \Phi_{H\,ILR})^{1/4}$
0
1
2
3
4
5
6
-4000
-2000
0
2000
4000
Velocity (km s^{-1})